The Astrophysical Journal, 613:580–591, 2004 September 20

EXTREME-ULTRAVIOLET AND X-RAY SPECTROSCOPY OF A SOLAR FLARE LOOP OBSERVED AT HIGH TIME RESOLUTION: A CASE STUDY IN CHROMOSPHERIC EVAPORATION

Jeffrey W. Brosius
Catholic University of America at NASA Goddard Space Flight Center, Code 682, Greenbelt, MD 20771

and

Kenneth J. H. Phillips[1]
NASA Goddard Space Flight Center, Code 682, Greenbelt, MD 20771
Received 2004 April 5; accepted 2004 May 27

ABSTRACT

We present extreme-ultraviolet (EUV) and X-ray light curves and Doppler velocity measurements for a *GOES* class M2 solar flare observed in NOAA Active Region 9433 on 2001 April 24 at high time resolution with the Coronal Diagnostic Spectrometer (CDS) on board the *Solar and Heliospheric Observatory* (*SOHO*) satellite (9.83 s) and the Bragg Crystal Spectrometer (BCS) and Hard X-Ray Telescope (HXT) on board the *Yohkoh* satellite (9.00 s). Coordinated imagery with *SOHO*'s Extreme-ultraviolet Imaging Telescope and the *Transition Region and Coronal Explorer* satellite reveal that the CDS slit was centered on the flare commencement site; coordinated magnetograms from *SOHO*'s Michelson Doppler Imager are consistent with this site being the footpoint of a flare loop anchored in positive magnetic field near the outer edge of a sunspot's penumbra. CDS observations include the preflare quiescent phase, two precursors, the flare impulsive and peak phases, and its slow decline. We find that (1) the average wavelengths of O III, O IV, O V, Ne VI, and He II lines measured during the preflare quiescent phase are equal (within the measurement uncertainties) to those measured during the late decline phase, indicating that they can be used as reference standards against which to measure Doppler velocities during the flare; (2) the EUV lines of O III, O IV, O V, and He II exhibit upflow velocities of $\sim$40 km s^{-1} during both precursor events, suggestive of small-scale chromospheric evaporation; (3) the Fe XIX EUV intensity rises and stays above its preflare noise level during the second (later) precursor; (4) the maximum upflow velocities measured in Fe XIX with CDS (64 km s^{-1}) and in Ca XIX (65 km s^{-1}) and S XV (78 km s^{-1}) with BCS occur during the flare impulsive phase and are simultaneous within the instrumental time resolutions; (5) the Fe XIX EUV intensity begins its impulsive rise nearly 90 s later than the rise in intensities of the cooler lines; (6) hard X-ray emission arises nearly 60 s after the cool EUV lines begin their impulsive intensity rise; and (7) the EUV lines of O III, O IV, O V, and He II exhibit downflow velocities of $\sim$40 km s^{-1} during the flare impulsive phase, suggesting momentum balance between the hot upflowing material and the cool downflowing material. Our observations are consistent with energy transport by nonthermal particle beams in chromospheric evaporation theory.

Subject headings: Sun: activity — Sun: corona — Sun: flares — Sun: X-rays, gamma rays — Sun: UV radiation

Online material: color figures

1. INTRODUCTION

It is well known from *Solar Maximum Mission* (*SMM*), *Yohkoh*, and earlier satellite observations that solar flare impulsive-phase soft X-ray emission lines from highly ionized ions formed at temperatures $\gtrsim 10^7$ K exhibit strongly blueshifted components corresponding to average upflow velocities of $\sim$300 km s^{-1} (Antonucci et al. 1982, 1999 and references therein; Zarro et al. 1988a; Fludra et al. 1989; Canfield et al. 1990; Doschek 1990; Mariska et al. 1993; Mariska 1994). These velocities have frequently been interpreted as evidence for "chromospheric evaporation" (Neupert 1968; Antonucci & Dennis 1983; Silva et al. 1997; Bornmann 1999 and references therein), wherein chromospheric material is heated by beamed particles and/or a thermal conduction front much more quickly than it can radiatively cool during the flare impulsive phase. As the material heats, it expands rapidly upward (hence the blueshifts) into the lower density corona and slowly downward into the higher density chromosphere.

The Bent Crystal Spectrometer (BCS) portion of the X-Ray Polychromator (XRP; Acton et al. 1980) on board *SMM* (operational 1980–1989) obtained spatially unresolved (6′ FWHM) soft X-ray spectra covering Ca XIX, Fe XXV, and Fe XXVI line emission, while the Flat Crystal Spectrometer (FCS) portion of XRP obtained spatially resolved ($<15''$) images at the peak-intensity wavelengths of strong spectral lines, most of which are formed at lower temperatures than those observed with BCS. The FCS was used primarily as an imaging device, and flare line profiles were obtained on only a few occasions (e.g., Zarro et al. 1988b). The Ultraviolet Spectrometer/Polarimeter (UVSP; Woodgate et al. 1980, Cheng 1999) on board *SMM* observed transition-region lines of O IV, O V, and Si IV, as well as a forbidden line of Fe XXI. In its "raster-through-the-line" mode, UVSP obtained spectroheliograms in a sequence of wavelengths, thus enabling the construction of line profiles in each spatial pixel from the successive wavelength images. However, because the spectroheliograms were sequential (not simultaneous) the reconstructed line profiles were not instantaneous. Thus no reliable measurements of impulsive-phase blueshifts or nonthermal broadening are available from UVSP.

[1] NRC Senior Research Associate.

The Bragg Crystal Spectrometer (BCS; Culhane et al. 1991) on board *Yohkoh* (operational 1991–2001) was approximately 10 times as sensitive as previous similar instruments. It obtained soft X-ray spectra covering Ca XIX, Fe XXV, and Fe XXVI lines (similar to *SMM*'s BCS), but it also included S XV. Although its whole-Sun field of view ensured that it observed every flare on the disk within its sensitivity range during any given observing period, it provided no spatial resolution.

The Coronal Diagnostic Spectrometer (CDS; Harrison et al. 1995) on board the *Solar and Heliospheric Observatory* (*SOHO*) satellite (launched in 1995 and still in operation as of this writing) contains a normal incidence spectrometer (NIS) that can be used to obtain instantaneous stigmatic extreme ultraviolet (EUV) spectra within its 308–381 Å (NIS-1) and 513–633 Å (NIS-2) wavebands for each of 143 1.″68 spatial pixels along its 4′ long slit. Several slit widths are available, the most commonly used being 4″. The instrument can be operated in a sit-and-stare mode wherein successive exposures over small (single-slit) areas are obtained, or it can be used to obtain raster images of target areas by obtaining spectra from successive slit pointings. To reduce readout time, subsets of the CDS wavebands can be selected, and data can be compressed (averaged) into fewer spatial pixels along the slit.

Czaykowska et al. (1999) obtained CDS raster images of a *GOES* class M6.8 flare in NOAA Active Region (AR) 8210 on 1998 April 29 during the late gradual phase. Their observations, which began nearly 1 hr after the soft X-ray peak, enabled them to map the relative Doppler velocities of O V, Fe XVI, and Fe XIX lines with a cadence of about 9 minutes. They interpret their observed pattern of relative upflows and downflows to indicate the presence of reconnection-driven chromospheric evaporation late in the flare's decay phase. Pike & Mason (2002) indirectly observed a *GOES* class X2.3 flare in NOAA AR 9415 on 2001 April 10 with CDS in its daily synoptic mode. This mode, which builds a series of nine $4' \times 4'$ rasters centered on the central meridian in several wavebands, was not designed for flare studies. In fact, CDS was not rastering over the flaring region during the flare itself, but was building the raster south and east of it. Pike & Mason (2002) focus primarily on profiles of the O V line at 629.7 Å. They find that multiple components, including a highly blueshifted one corresponding to line-of-sight velocities in excess of 400 km s^{-1}, are required to obtain the best fit to the spectra.

The CDS observing sequence PBEAM was developed to obtain rapid cadence spectra over 549–559 and 590–631 Å subsets of the NIS-2 waveband by compressing $4'' \times 240''$ slit spectra into twelve $4'' \times 20''$ pixels (Brosius 2001, 2003). Although the exposure time is only 1.5 s, the net time resolution is readout-limited to 9.83 s. The slit was centered on NOAA AR 9502 on 2001 June 15 during a *GOES* class M6.3 flare, yielding spatially unambiguous, high time resolution spectra before, during, and long after the impulsive phase. Brosius (2003) focused on the four strong EUV lines of O III at 599.6 Å, O V at 629.7 Å, Mg X at 624.9 Å, and Fe XIX at 592.2 Å. He found that the profiles of all four lines became blueshifted during the impulsive rise of the flare, but only the three cooler lines (those of O III, O V, and Mg X) exhibited multiple highly blueshifted components (with Doppler velocities of ~800 km s^{-1}), and subsequently exhibited redshifts. He noted that the O III and O V emission exhibit a pronounced precursor brightening during which the Fe XIX emission emerged above the noise; this, combined with the fact that the O III and O V intensities began their impulsive rise earlier than did those of Mg X and Fe XIX, is consistent with the transport of coronal flare energy to the chromosphere by nonthermal particle beams. He concluded that this provided strong evidence for chromospheric evaporation followed by "warm rain."

The PBEAM study was run on NOAA AR 9433 on 2001 April 24 during a *GOES* class M2.3 flare. We were fortunate to have had the slit centered on the commencement site of a flare loop before, during, and long after the impulsive phase. The *Yohkoh* satellite was in daylight outside the South Atlantic Anomaly (SAA) during this event, and it provides coordinated soft X-ray and hard X-ray observations. Some results from these unique observations are presented in this paper. In § 2 we describe our observations and data reduction procedures, in § 3 we present results of our spectroscopic measurements of flare light curves and bulk flows, in § 4 we discuss implications of our results, and in § 5 we summarize our findings.

2. OBSERVATIONS AND DATA REDUCTION

We observed NOAA AR 9433 (N24°, E10°) with *SOHO*'s CDS between 17:34 UT on 2001 April 24 and 01:13 UT on 2001 April 25. Here we focus on 1 hour's observations centered roughly on the *GOES* class M2.3 flare that started at 18:04 UT and peaked at 18:12 UT; we obtained coordinated observations with *SOHO*'s Extreme-ultraviolet Imaging Telescope (EIT; Delaboudinière et al. 1995), *SOHO*'s Michelson Doppler Imager (MDI; Scherrer et al. 1995), the *Transition Region and Coronal Explorer* (*TRACE*) satellite (Handy et al. 1999), *Yohkoh*'s BCS, and *Yohkoh*'s Hard X-ray Telescope (HXT; Kosugi et al. 1991) during this event.

2.1. *SOHO's EIT*

As part of its ongoing solar monitoring program, *SOHO*'s EIT acquires full-Sun images every 12 minutes in its 195 Å waveband. This waveband is nearly always dominated by emission from Fe XII (whose maximum ionization fraction occurs at $T_m = 1.3 \times 10^6$ K, or $\log T_m = 6.1$) over most of the solar corona; however, during a flare, Fe XXIV emission ($\log T_m = 7.3$) at 192 Å is also likely to contribute. Figure 1 shows a sequence of six $4' \times 4'$ 195 Å EIT images extracted from the full-Sun images obtained during our observing run. The pixel size is 2.″62. Intensities in all six frames are normalized to the maximum value in the first frame of the series. The $4'' \times 240''$ CDS slit, divided into twelve $4'' \times 20''$ pixels, is superposed on each image. Images (Sato et al. 2003) obtained with *Yohkoh*'s Soft X-ray Telescope (SXT; Tsuneta et al. 1991) appear very similar to the EIT images and are not shown here.

An extended flare loop is clearly visible in the last three frames of the sequence. Of greatest interest for what follows, however, are the small bright sources that appear at 17:48 UT, labeled A and B in the second frame of Figure 1. Source A lies within the seventh CDS slit pixel up from the bottom in Figure 1. We focus on EUV spectra from this pixel in this investigation.

2.2. *SOHO's MDI*

We obtained a full disk 1.″98 pixel photospheric longitudinal magnetogram at 17:48 UT, and a full-disk 1.″98 pixel visible continuum intensity image at 17:36 UT, with *SOHO*'s MDI. See Figure 2, where the left frame shows a $140'' \times 140''$ EIT image (obtained at 17:48 UT) with photospheric longitudinal magnetic field contours of +150 G (*solid lines*) and −150 G (*dashed lines*), and the right frame shows the co-aligned MDI continuum intensity image with EIT intensity contours to indicate the locations of the flare commencement sources A and B. A large sunspot is present north and west of the center in

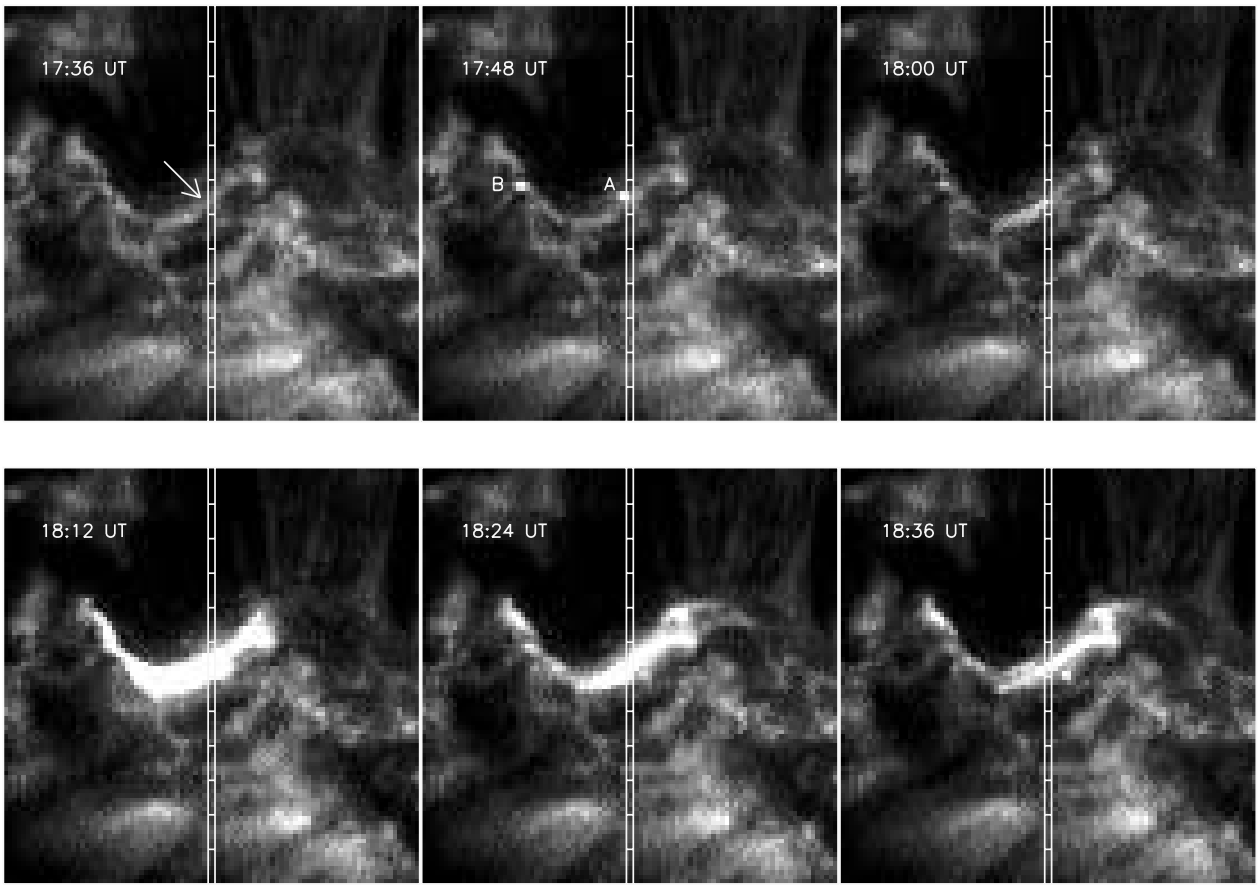

FIG. 1.—Sequence of $4' \times 4'$ EIT 195 Å images obtained between 17:36 and 18:36 UT on 2001 April 24, showing the location of the $4' \times 4'$ CDS slit within NOAA AR 9433. Horizontal tick marks indicate the endpoints of the twelve $4'' \times 20''$ spatial pixels into which the CDS spectra were compressed. The times at which the images were obtained are given in the upper left corner of each frame. Spectral data described and analyzed in this work were obtained in the seventh slit pixel up from the bottom, indicated with an arrow at 17:36 UT. Flare sources A and B are indicated at 17:48 UT. Solar north is up, and west is to the right. [*See the electronic edition of the Journal for a color version of this figure.*]

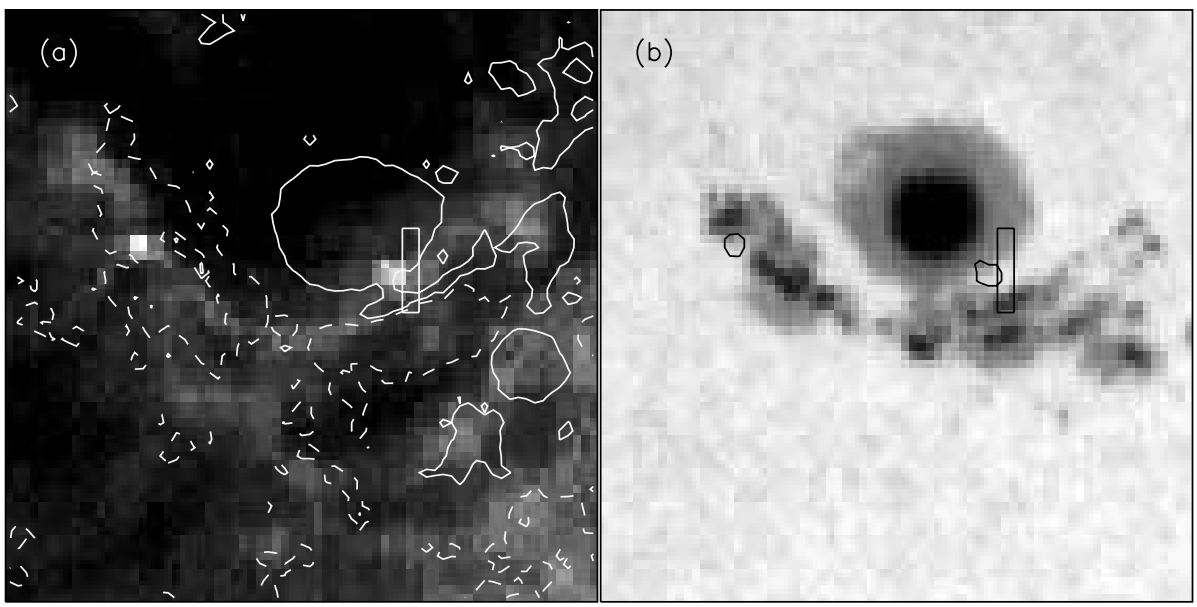

FIG. 2.—(*a*) $140'' \times 140''$ EIT 195 Å image obtained at 17:48 UT, showing photospheric longitudinal magnetic field contours of +150 G (*solid line*) and −150 G (*dashed line*) obtained simultaneously with MDI. (*b*) $140'' \times 140''$ MDI visible continuum intensity image (obtained at 17:36 UT and shifted $\sim 2''$ to co-align with [*a*]) with EIT intensity contours showing the location of the flare loop footpoints. The narrow vertical rectangle shows the location of the $4'' \times 20''$ CDS slit pixel from which the spectra presented in this work were obtained. Solar north is up, and west is to the right. [*See the electronic edition of the Journal for a color version of this figure.*]

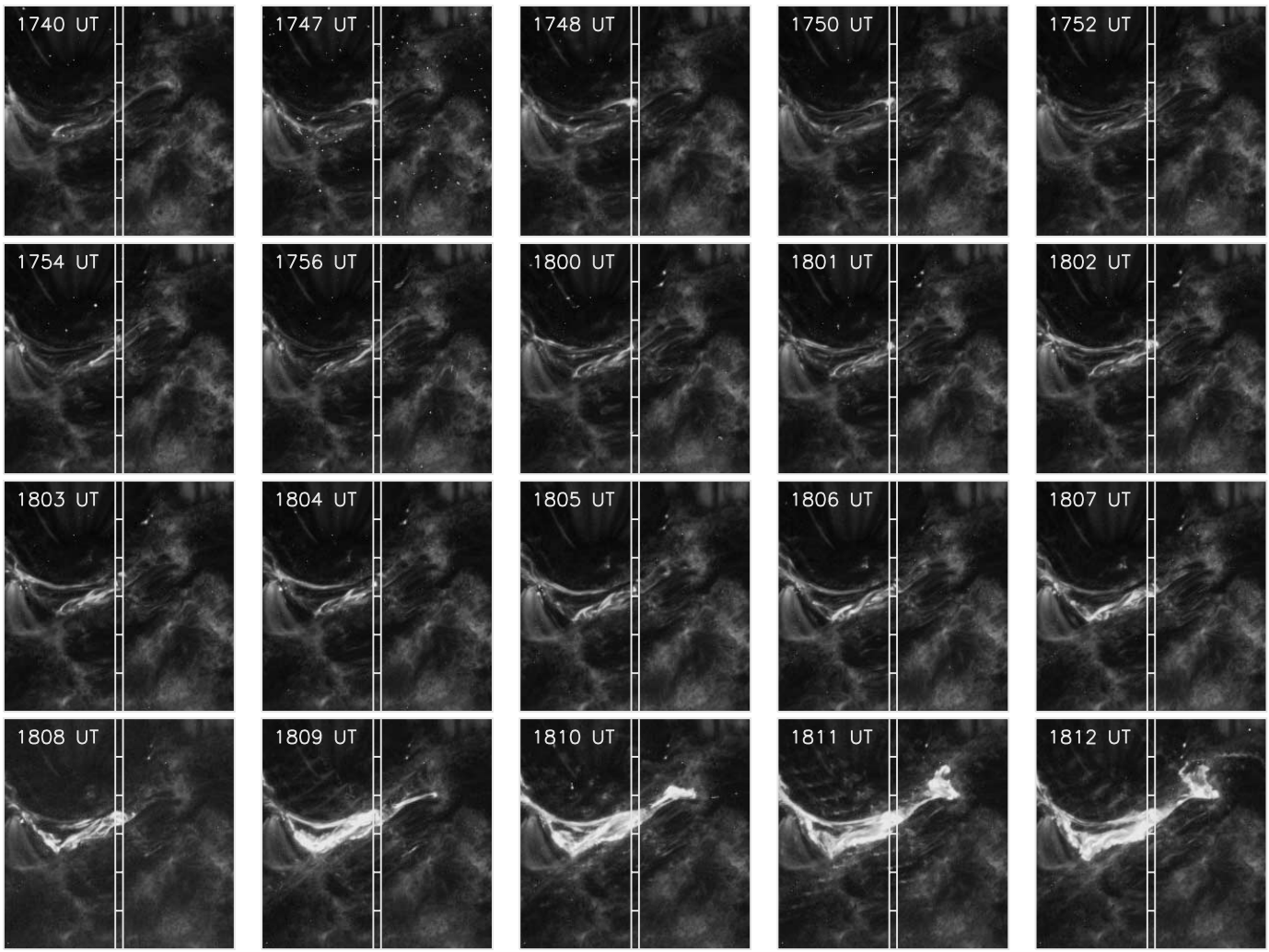

FIG. 3.—Sequence of $2' \times 2'$ TRACE 171 Å images obtained between 17:40 and 18:12 UT on 2001 April 24, showing the location of the CDS slit within NOAA AR 9433. Horizontal tick marks indicate the endpoints of the $4'' \times 20''$ spatial pixels into which the CDS spectra were compressed. The times at which the images were obtained are given in the upper left corner of each frame. Spectral data described and analyzed in this work were obtained in the fourth slit pixel up from the bottom, which corresponds to the seventh pixel in Fig. 1. Solar north is up, and west is to the right. [*See the electronic edition of the Journal for a color version of this figure.*]

each frame. The continuum intensity image was shifted $\sim 2''$ to compensate for solar rotation during the 12 minute time difference between it and the EIT image (and MDI magnetogram) at 17:48 UT. Also displayed on both frames is the seventh $4'' \times 20''$ CDS slit pixel up from the bottom in Figure 1 (where it is labeled A). It is important to note that the brightenings observed with EIT occur in areas of oppositely directed magnetic field, consistent with their being conjugate footpoints of the flare loop. Footpoint A is located in the CDS field of view within a narrow strip that seems to form a gap in the penumbra.

2.3. *TRACE*

The *TRACE* satellite obtained a variable-cadence sequence of $6.'40 \times 6.'40$ images in its 171 Å waveband during our observing period. This waveband is dominated by emission from Fe IX, whose maximum ionization fraction occurs at $\log T_m = 5.9$. Figure 3 shows a sequence of twenty $2' \times 2'$ 171 Å *TRACE* images covering the period 17:40–18:12 UT. These images provide a more comprehensive picture of the time evolution of the flaring region than can be gleaned from the EIT images alone. Intensities in all *TRACE* images have been compensated for different exposure times and normalized to a common intensity scale. The pixel size is $0.''5$. A careful co-alignment between the *TRACE* and full-Sun EIT images revealed that the *TRACE* images needed to be shifted by $-6.''5$ in the x-direction and $-8.''0$ in the y-direction relative to the nominal pointings listed in the data file headers. Once this adjustment was made, the $4'' \times 20''$ CDS slit pixels corresponding to the $2' \times 2'$ *TRACE* images in Figure 3 were superposed. Note that the small bright source A from which the flare commences (the seventh CDS slit pixel up from the bottom in Fig. 1) is in the fourth CDS slit pixel up from the bottom in Figure 3. The sequences of EIT and *TRACE* images reveal that the flare commencement site is located well within the field of view of the CDS slit during our observations. Further, they show that the flare loop exhibits complex structure with significant extension both west of source A and east of source B, but does not disrupt.

2.4. *SOHO's CDS*

A total of 2800 spectra, each covering the wavelength ranges 549–559 Å and 590–631 Å, were obtained for every one of the twelve $4'' \times 20''$ slit pixels during the 7.65 hr observing period.

TABLE 1
PREFLARE AND LATE-PHASE AVERAGE PARAMETERS OF EUV LINES

		Preflare Values			Late-Phase Values		
Ion	log T_m	Wavelength	Width	Intensity	Wavelength	Width	Intensity
He II	4.7	303.781 ± 0.006	0.2800 ± 0.0114	43480 ± 3738	303.782 ± 0.004	0.2905 ± 0.0099	88260.0 ± 11140.0
O III	5.0	599.605 ± 0.032	0.5284 ± 0.0506	210.2 ± 42.2	599.606 ± 0.016	0.5601 ± 0.0327	427.6 ± 55.5
O IV	5.2	554.350 ± 0.035	0.5590 ± 0.0376	1422 ± 240	554.357 ± 0.017	0.5837 ± 0.0218	2808.0 ± 363.0
O V	5.4	629.761 ± 0.017	0.5012 ± 0.0171	2383 ± 227	629.765 ± 0.008	0.5189 ± 0.0105	5088.0 ± 614.0
Ne VI	5.6	558.571 ± 0.040	0.5190 ± 0.0859	80.7 ± 20.2	558.591 ± 0.024	0.5789 ± 0.0535	234.0 ± 40.6
Mg X	6.1	609.766 ± 0.005	0.5229 ± 0.0102	1899 ± 53.7	609.789 ± 0.004	0.5270 ± 0.0088	3641.0 ± 102.0
Mg X	6.1	624.941 ± 0.009	0.5393 ± 0.0207	689.0 ± 32.7	624.966 ± 0.006	0.5538 ± 0.0173	1193.0 ± 48.0
Fe XIX	6.9	...	...	42.0 ± 17.9	592.232 ± 0.009	0.5548 ± 0.0201	932.6 ± 80.2

NOTES.—T_m is the temperature (in K) that maximizes the ionization fraction of the relevant ion (e.g., Mazzotta et al. 1998). Wavelengths and widths are in Å; intensities are in ergs cm^{-2} s^{-1} sr^{-1}. Preflare average values are derived from spectra obtained between 17:36 and 17:44 UT; late-phase values are derived from spectra obtained between 18:30 and 18:36 UT.

One full set of spectra was obtained every 9.83 s, the CDS time resolution for this study. The CDS pointing was fixed at ($x = -165''$, $y = +385''$), so that the observed solar features slowly drifted across the CDS field of view because of solar rotation. The CDS spectra were processed and calibrated using standard SolarSoftware IDL procedures. A comparison between the slit spectra and the EIT images indicates that the CDS pointing was accurate to better than its nominal $15''$ uncertainty. Figures 1, 2, and 3 show the pointing of the CDS slit relative to EIT, MDI, and *TRACE* images.

We used the "broadened Gaussian" line profile fitting procedure developed by Thompson (1999) to obtain profile fits to selected lines in our spectra. This procedure, which differs from the standard Gaussian profile fitting procedure, was developed because CDS line profiles were found to deviate noticeably from Gaussians after the loss of *SOHO* attitude control in 1998. Thompson's procedure calculates an amplitude (A), centroid wavelength (λ), and "broadened width" (w, effectively the FWHM), similar to the standard Gaussian profile fit procedure; in addition, it incorporates red-wing and blue-wing asymmetry parameters, both of which are normally held constant but can be allowed vary if desired. Based on Thompson's (1999) procedure, the integrated intensities of our spectral lines can be written $I = 1.485Aw$. We fit "broadened Gaussian" profiles to the lines of O III at 599.6 Å, a blend of four O IV lines around 554 Å, O V at 629.7 Å, Ne VI at 558.6 Å, Mg X at 609.8 and 624.9 Å, Fe XIX at 592.2 Å, and He II at 303.8 Å (seen in second order at 607.6 Å). For O IV, where we fit four blended profiles, the total integrated intensity is the sum of the integrated intensities of the four components. The temperatures T_m (in K) that maximize the fractional ion abundances for these lines (e.g., Mazzotta et al. 1998) are given in Table 1.

We were fortunate to have had the CDS slit located over the flare commencement site beginning nearly a half-hour before the *GOES* class M2.3 flare that peaked at 18:12 UT. See Figure 1, where the compact bright source A in the EIT image at 17:48 UT is in the seventh pixel up from the bottom of the $4'$ long CDS slit; this same source is evident in Figure 2 and in the fourth pixel up from the bottom of the *TRACE* images in Figure 3. In this work we focus on spectra from this single $4'' \times 20''$ CDS slit pixel. The timing of our observations enabled us to obtain EUV spectra during the preflare quiescent period, two precursor events, the flare impulsive phase, the flare peak, and its slow decline. We use the integrated intensities and centroid wavelengths to display EUV light curves and time histories of the EUV Doppler velocities. Doppler velocities are derived from wavelength shifts relative to average values obtained during the preflare quiescent period and the late slow decline period (Table 1; see Figs. 4 and 5). These are analyzed and discussed in detail below.

2.5. *Yohkoh's BCS*

The *Yohkoh* satellite was in daylight outside the SAA from about 17:54–18:54 UT, so we can directly compare the spatially resolved CDS EUV flare source spectra with coordinated full-Sun BCS soft X-ray spectra during various phases of this event. We used standard SolarSoftware *Yohkoh* BCS IDL procedures to fit profiles to the S XV line at 5.039 Å ($\log T_m = 6.8$) and the Ca XIX line at 3.177 Å ($\log T_m = 7.1$). The Fe XXV line at 1.850 Å ($\log T_m = 7.6$) is weak and too noisy to be used in this work. The BCS soft X-ray light curves are displayed in the lower right frame of Figure 4. These are the total count rates in the Ca XIX and S XV channels, including small contributions from continuum emission. The corresponding Doppler velocities for Ca XIX are displayed in the lower right frame of Figure 5. (We do not overplot velocities for S XV in order to avoid confusion.) We used the average wavelength measured during the late decline phase of the flare to establish the "standard" against which Doppler velocities were calculated. The BCS time resolution for this study was 9.00 s.

2.6. *Yohkoh's HXT*

We used standard SolarSoftware *Yohkoh* HXT IDL procedures to obtain full-Sun light curves for each of the four hard X-ray energy channels: L (13.9–22.7 keV), M1 (22.7–32.7 keV), M2 (32.7–52.7 keV), and H (52.7–92.8 keV). These are shown in Figure 6, which includes BCS light curves for comparison. Sato et al. (2003) show hard X-ray images for all but the highest energy channel for this event. The hard X-ray emission in these images covers less than half the length of the flare loop seen in EUV (and soft X-ray) emission and is centered near the flare commencement site (source A in Fig. 1).

3. RESULTS

Figure 4 shows light curves, i.e., time histories of the logarithm of the integrated line intensity (ergs cm^{-2} s^{-1} sr^{-1}) for He II, O III, O IV, O V, Ne VI, Mg X, and Fe XIX; the last frame shows a similar plot of the total count rates in the BCS S XV

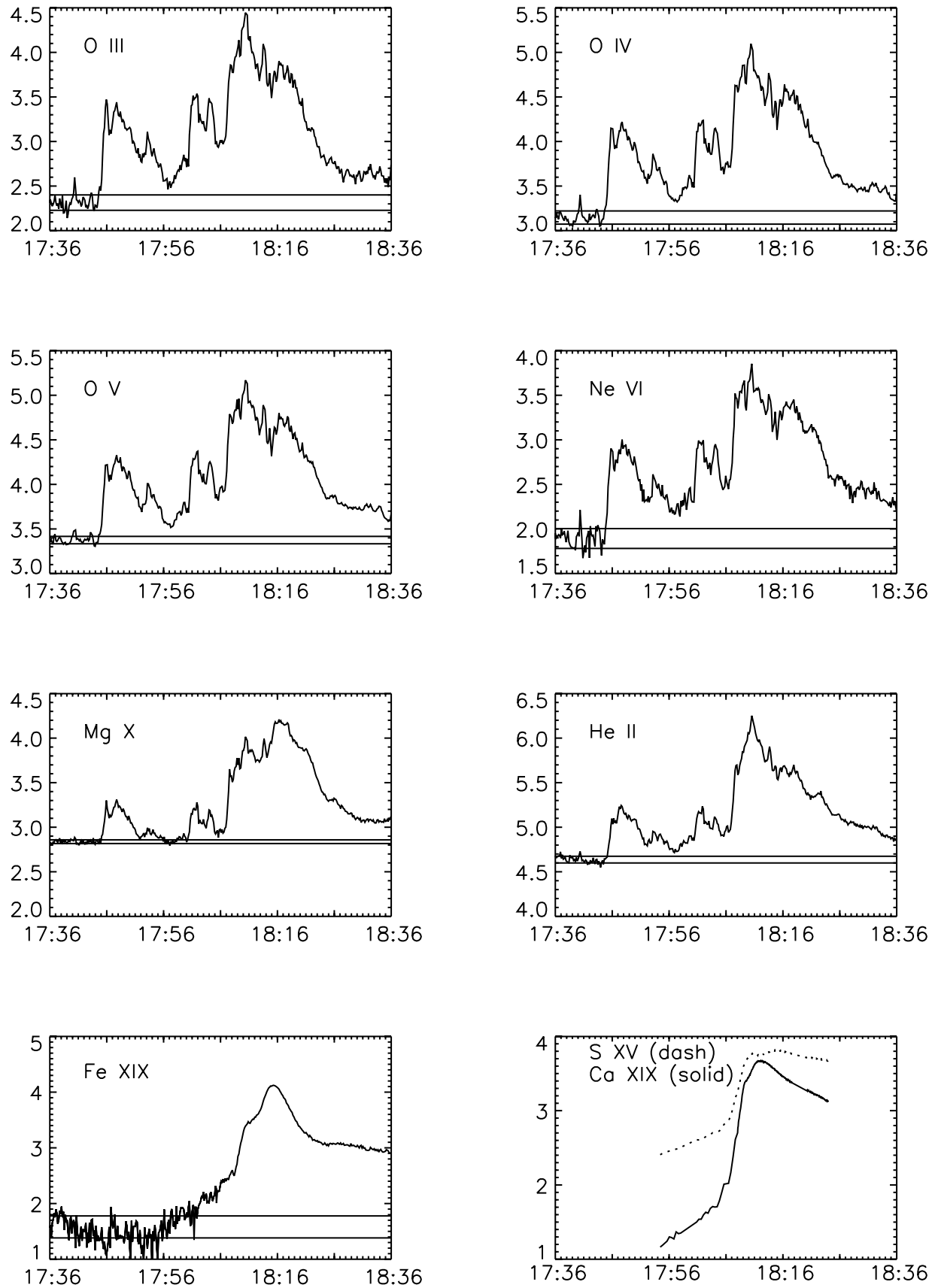

FIG. 4.—Logarithms of the integrated line intensities in ergs cm^{-2} s^{-1} sr^{-1} for O III, O IV, O V, Ne VI, Mg X, He II, and Fe XIX as functions of time UT measured with *SOHO*'s CDS in the flare commencement site (source A in Fig. 1). Solid horizontal lines indicate preflare quiescent average values ± 1 σ. The bottom right frame shows the logarithms of the total count rates for S XV and Ca XIX measured with *Yohkoh*'s BCS for a full-Sun field of view.

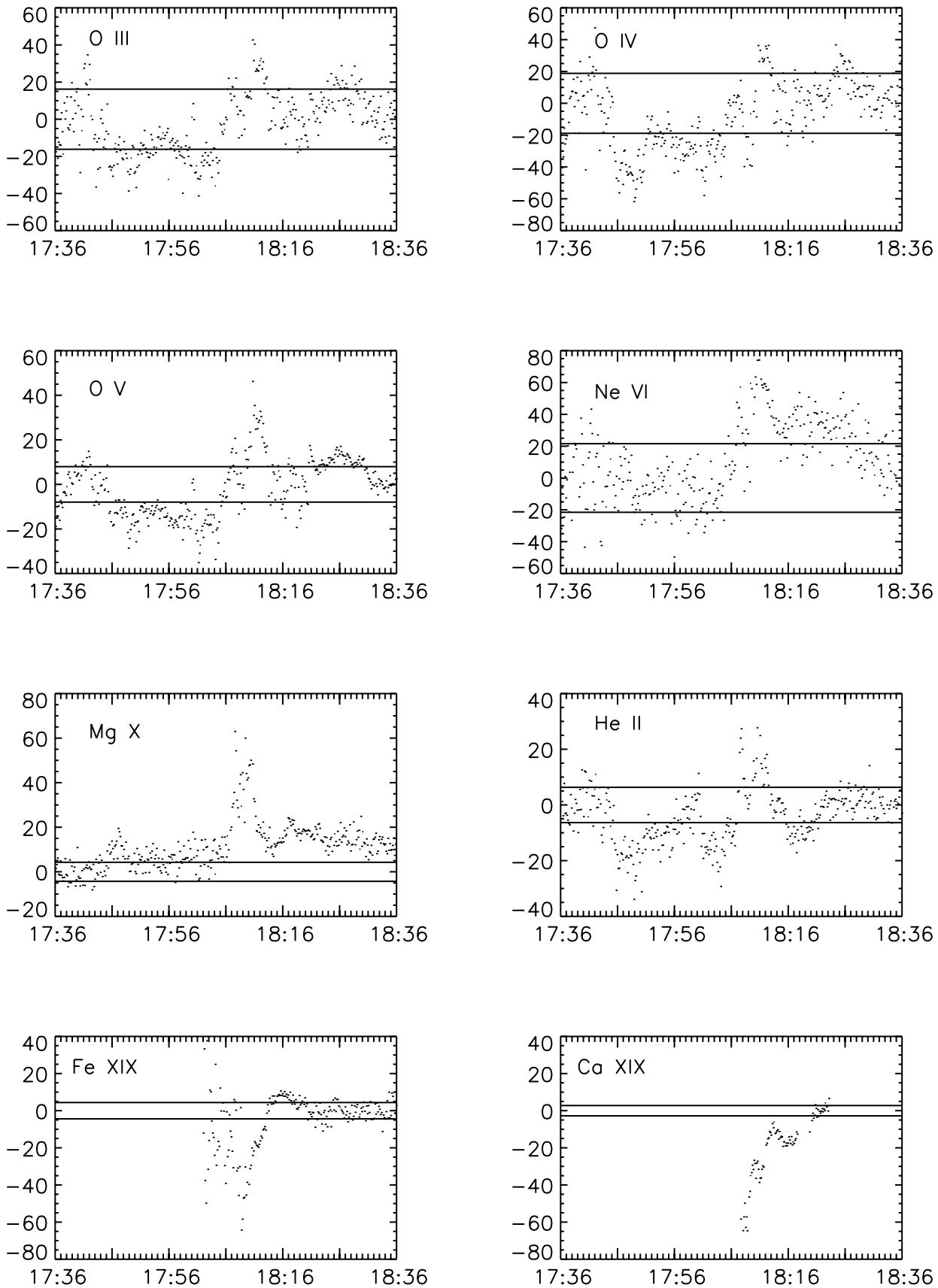

FIG. 5.—Doppler velocities in km s^{-1} for O III, O IV, O V, Ne VI, Mg X, He II, and Fe XIX as functions of time UT measured with *SOHO*'s CDS in the flare commencement site (source A in Fig. 1). Negative velocities correspond to upflows (blueshifts) and positive to downflows (redshifts). Solid horizontal lines indicate $\pm 1\ \sigma$ from rest. The bottom right frame shows the velocity for Ca XIX measured with *Yohkoh*'s BCS for a full-Sun field of view.

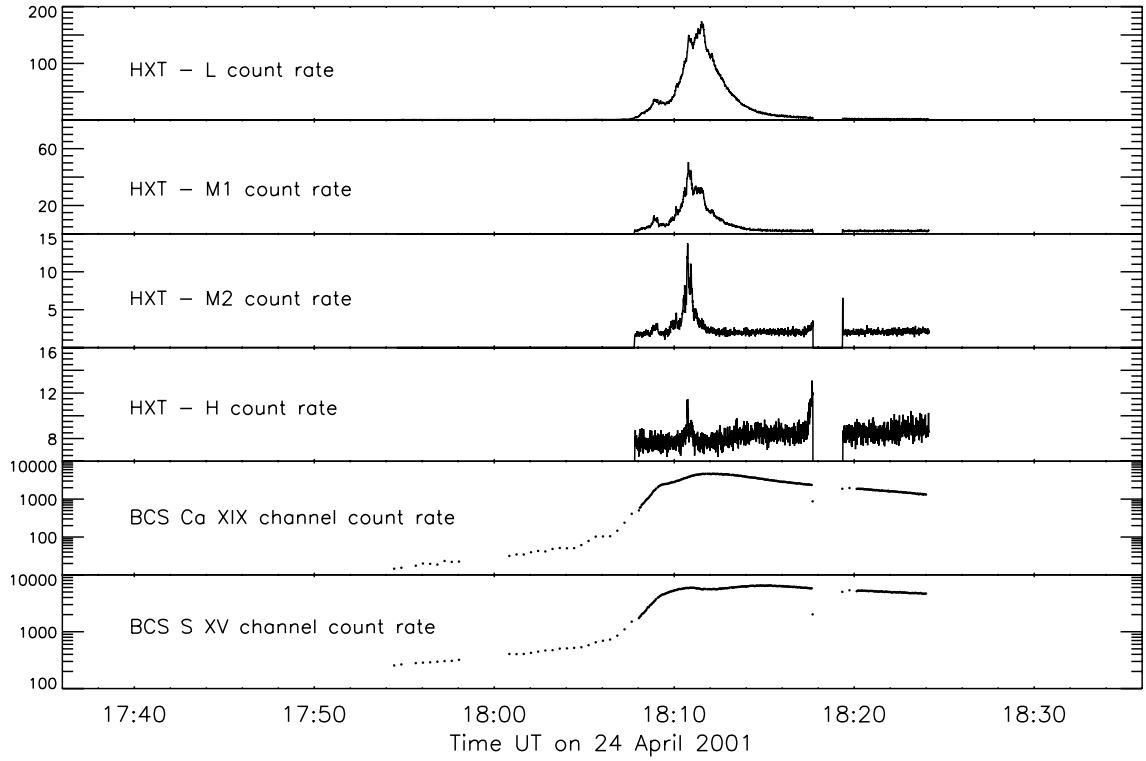

FIG. 6.—Full-Sun light curves (count rates) derived from the four hard X-ray channels of *Yohkoh*'s HXT, and the Ca XIX and S XV channels of BCS. Although *Yohkoh* observations began at 17:54:20 UT, statistically significant hard X-ray count rates did not begin until 18:07:40 UT. The Ca XIX and S XV light curves include continuum contributions as well as emission lines.

and Ca XIX channels. Light curves for the first six lines in Figure 4, all of which have maximum ionization fractions at $T_m \lesssim 1 \times 10^6$ K (and are hereafter frequently referred to as "cooler lines;" see Table 1), reveal (1) a preflare quiescent phase extending from the beginning of our observations to about 17:44 UT, (2) two precursor events (17:44:30–17:57:10 and 18:00:30–18:05:30 UT), (3) an impulsive intensity rise beginning around 18:06:50 UT, (4) an intensity peak at 18:10:20, and (5) a period of variability and rapid postflare decline ending around 18:24:30 UT, followed by a period of much more gradual postflare decline. Although the Fe XIX emission is weak and extremely noisy, it appears to be declining during the preflare quiescent period. This is possibly remnant emission from a *GOES* class M1.6 flare that ended nearly 5 hr earlier. It exhibits a small enhancement during the first precursor and then appears to begin a slow steady rise either late during the first precursor or early during the second. In any case, it rises and stays above its preflare noise level during the second precursor. The Fe XIX impulsive intensity rise begins around 18:08:20 UT (1.5 minutes later than that of the cooler lines), and its intensity peak occurs at 18:15:20 UT (5.0 minutes later than that of the cooler lines). The variability exhibited by the cooler lines during the period of rapid postflare decline is not present in this or the S XV and Ca XIX lines. A slow rise in both the Ca XIX and S XV emission is already in progress when BCS observations begin at 17:54:30 UT (late during the first EUV precursor). The Ca XIX channel exhibits its peak count rate at 18:12:08 UT, simultaneously with the *GOES* soft X-ray peak. The S XV channel shows an initial peak at 18:10:53 UT (about a half minute after the peak intensity of the cool EUV lines), a relative minimum at 18:11:35 UT, and its main peak at 18:14:47 UT (about a half-minute earlier than that of Fe XIX). That these peaks are not simultaneous with the Fe XIX peak is likely due to the fact that the S XV, Ca XIX, and *GOES* soft X-rays are measured over the whole Sun, not just the flare commencement site within the CDS field of view.

Hard X-ray light curves are shown in Figure 6. Significant emission in the L channel began at 18:07:48 UT, nearly 20 minutes after the initial precursor brightening observed with EIT, CDS, and *TRACE*, and nearly 1 minute after the impulsive intensity rise of the cool EUV lines. A short-lived "spike" was observed by HXT in all four channels at 18:10:40 UT, long after the cool EUV lines began their impulsive intensity rise (18:06:50 UT), and shortly after they reached their peak-intensity values (18:10:20 UT). Emission in the L channel varies more gradually and ends later than it does in the higher energy channels; it reaches a maximum value at 18:11:30 UT (about 50 s later than the spike observed in all four hard X-ray channels and about 40 s earlier than the Ca XIX emission observed by BCS), and ends at about 18:17:30 UT.

Figure 7 displays light curves of O V and Fe XIX on an expanded scale and indicates various events during the observing sequence. This figure essentially provides a time line of key events in Figures 4 and 5 so that their relative sequence can be viewed at a glance. From left to right, the labeled lines include (*a*) the end of the preflare quiescent period (17:44 UT), (*b*) the onset of the first precursor (17:44:30 UT), (*c*) the end of the first precursor (17:57:10 UT), (*d*) the onset of the second precursor (18:00:30 UT), (*e*) the end of the second precursor (18:05:30 UT), (*f*) the impulsive intensity rise of the cool ($\log T_m \lesssim 6.0$) EUV lines (18:06:50 UT), (*g*) the impulsive intensity rise of Fe XIX (18:08:20 UT), (*h*) the peak intensity of the cool EUV lines (18:10:20 UT), (*i*) the peak intensity of Fe XIX (18:15:20 UT), (*j*) the beginning of the postflare gradual decline phase (18:24:30 UT), and (*k*) the beginning of the postflare period from which average values in Table 1 are

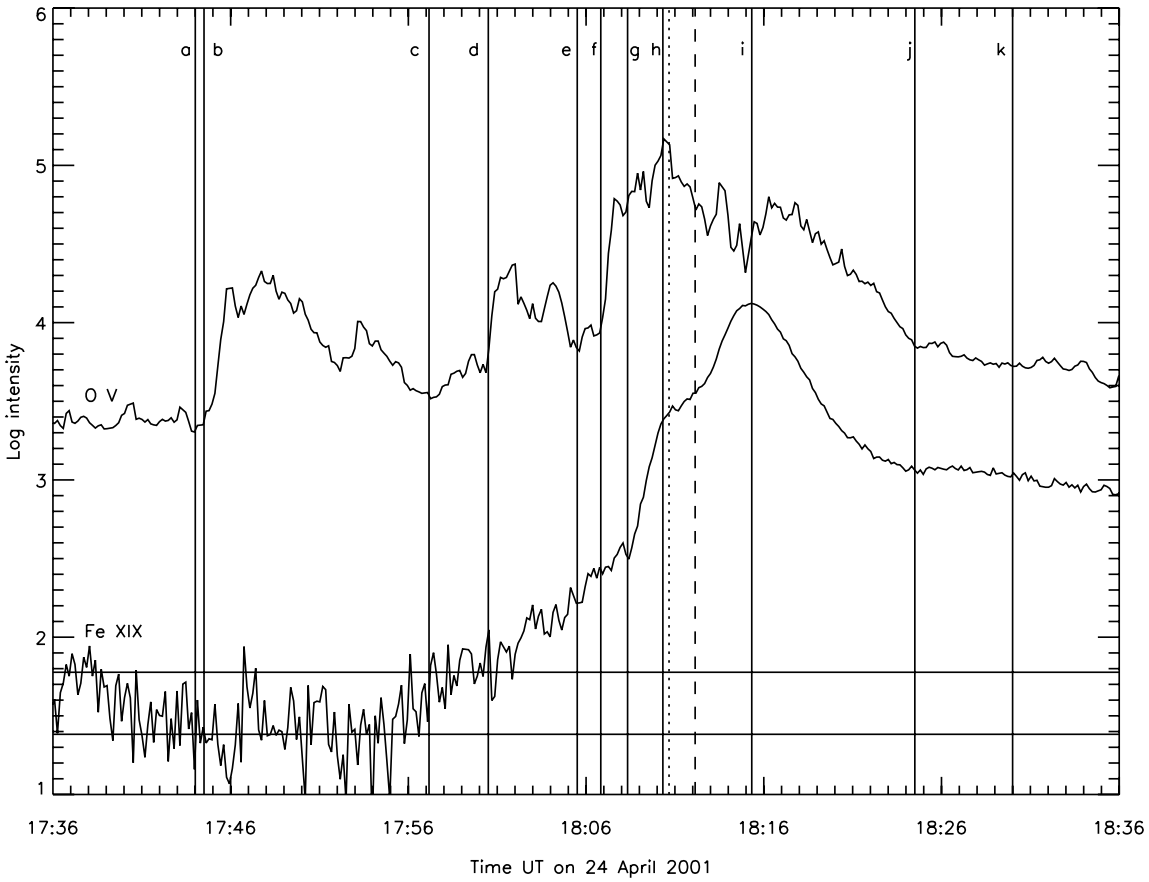

FIG. 7.—Light curves for O V (*top*) and Fe XIX (*bottom*) showing key events for this flare. Solid horizontal lines indicate the preflare quiescent average Fe XIX intensity (essentially noise) $\pm 1\ \sigma$. All times are UT. The solid vertical lines indicate the following: (*a*) the end of the preflare quiescent period (17:44); (*b*) the onset (17:44:30) and (*c*) end (17:57:10) of the first precursor; (*d*) the onset (18:00:30) and (*e*) end (18:05:30) of the second precursor; (*f*) the impulsive intensity rise of the cooler lines (18:06:50); (*g*) the impulsive intensity rise of Fe XIX (18:08:20); (*h*) the peak intensity of the cool EUV lines (18:10:20); (*i*) the peak intensity of Fe XIX (18:15:20); (*j*) the beginning of the postflare gradual decline phase (18:24:30); and (*k*) the beginning of the period from which average values in Table 1 are obtained (18:30). The unlabeled dashed line indicates the time of maximum soft X-ray emission observed in the BCS Ca XIX channel (18:12:08 UT), and the unlabeled dotted line indicates the time of the hard X-ray spike observed in all four of HXT's high-energy channels (18:10:40 UT). The maximum blueshift observed in Fe XIX occurs at 18:08:44 UT, near to the right of (*g*).

obtained (18:30 UT). Also shown is the time of the hard X-ray spike observed in all four of HXT's high-energy channels (an unlabeled dotted line at 18:10:40 UT) and the time of maximum soft X-ray emission observed in the BCS Ca XIX channel (as an unlabeled dashed line at 18:12:08 UT).

Table 1 lists the average wavelengths, widths, and integrated intensities derived from the time series of line profile fits to spectra obtained during the preflare quiescent period (17:36–17:44 UT) and postflare gradual decline (18:30–18:36 UT). For O IV we list intensity-weighted wavelengths and widths in which, for example, the average wavelength of the four component blend can be written $\lambda = (\lambda_1 I_1 + \lambda_2 I_2 + \lambda_3 I_3 + \lambda_4 I_4)/(I_1 + I_2 + I_3 + I_4)$. The uncertainties listed for each average value are the standard deviations derived from the time series of measured values. It is important to realize that the wavelengths measured by CDS are not absolutely calibrated, which means that differences between measured values and known standards are not significant. Notice, however, that (except for the Mg X lines) the preflare and postflare wavelengths and widths are equal to within their measurement uncertainties. A similar result was reported by Brosius (2003) for a *GOES* class M6 event, which indicates that plasma motions during the gradual decline phase settle back down to their preflare quiescent conditions. This means that we have reliable quiescent reference wavelengths against which to measure Doppler velocities in the flare plasma. Since the Mg X wavelengths during the gradual decline phase do not return to their preflare values but remain significantly redshifted, we do not consider the Doppler velocities measured in these lines to be as reliable as those in the other lines. While one possible explanation for this systematic redshift is simply that 10^6 K plasma continues to fall back down during the gradual decline phase, another is that the Mg X lines are significantly blended with lines of O IV. This will be discussed further in the next section.

Figure 5 shows the time history of the Doppler velocity (km s^{-1}) measured for He II, O III, O IV, O V, Ne VI, Mg X, Fe XIX, and Ca XIX. For He II through Mg X the solid horizontal lines indicate $\pm 1\ \sigma$ from the preflare quiescent (rest) values. For Fe XIX the solid horizontal lines indicate $\pm 1\ \sigma$ from the gradual decline (rest) value, and for Ca XIX they indicate $\pm 1\ \sigma$ from the average value derived late during the BCS observing period (18:20:08–18:23:08 UT). Fe XIX is so weak and noisy before the flare that we do not show Doppler velocity measurements at those times. Further, the Ca XIX and S XV spectra are so weak that it is not possible to obtain velocity measurements from them earlier than 18:08:20 UT, the start of the impulsive rise in Fe XIX emission. Notice that the He II, O III, O IV, and O V lines exhibit significant upflows (blueshifts) of $\sim$40 km s^{-1} during the two precursors. Mg X shows a small downflow (redshift) during the same time but, as discussed

below, Doppler velocity measurements with the Mg x lines may be unreliable because of blending with O IV lines. Ne VI, although somewhat noisy, also yields a barely significant blueshift during the precursors.

During the impulsive phase, the hot flare plasma intensity rises rapidly and shows a relatively strong blueshift. The maximum upflow velocity measured in Fe XIX with CDS is 64 km s^{-1} and occurs at 18:08:44 UT. The maximum upflow velocities measured in Ca XIX and S XV with BCS are 65 and 78 km s^{-1}, respectively, and occur at 18:08:47 and 18:08:38 UT. It is worth noting that these maximum measured upflow velocities are essentially simultaneous within the CDS (9.83 s) and BCS (9.00 s) time resolutions. The observed Doppler velocities remain well below the Sun's escape velocity (618 km s^{-1}), consistent with the fact that no CME or filament liftoff is observed. Since BCS observes the whole Sun while CDS observes only a small area around the flare commencement site, the simultaneity of the velocity peaks and the near-equality of their measured values indicate that the flare commencement site dominates the BCS measurements early during the flare impulsive phase. As the loop begins to fill and plasma outside the CDS field of view becomes more prominent, the flare commencement site itself no longer dominates the BCS flare spectra; thus the light curves and time histories of the BCS velocities eventually differ from those measured with CDS. A possible explanation for the time difference between the Fe XIX and Ca XIX (and S XV) intensity peaks may be that only after the upflowing material has filled the rest of the flare loop will it have the chance to fill the flare commencement site itself. In fact, this is when the Fe XIX emission begins to show a slight redshift, possibly indicating that the hot material that filled the loop has begun to fall back down into the footpoint.

Simultaneously with the upflows observed in the hot flare lines during the flare impulsive phase, all of the cooler EUV lines show significant downflows of $\sim$40 km s^{-1}. This is strong evidence for momentum balance between the hot upflowing plasma and cool downflowing plasma. See Figure 8, which compares the downflow (positive) velocities observed in He II and O V with the upflow (negative) velocities observed in Fe XIX. We have excluded the Fe XIX Doppler velocity measurements for times earlier than 18:06 UT from Figure 8 because the Fe XIX spectra at those times are weak and noisy and yield a fair amount of scatter in their measured velocities (see Fig. 5). Also evident in Figure 8 are the upflow velocities observed in the cooler lines during the second precursor (18:00:30–18:05:30 UT).

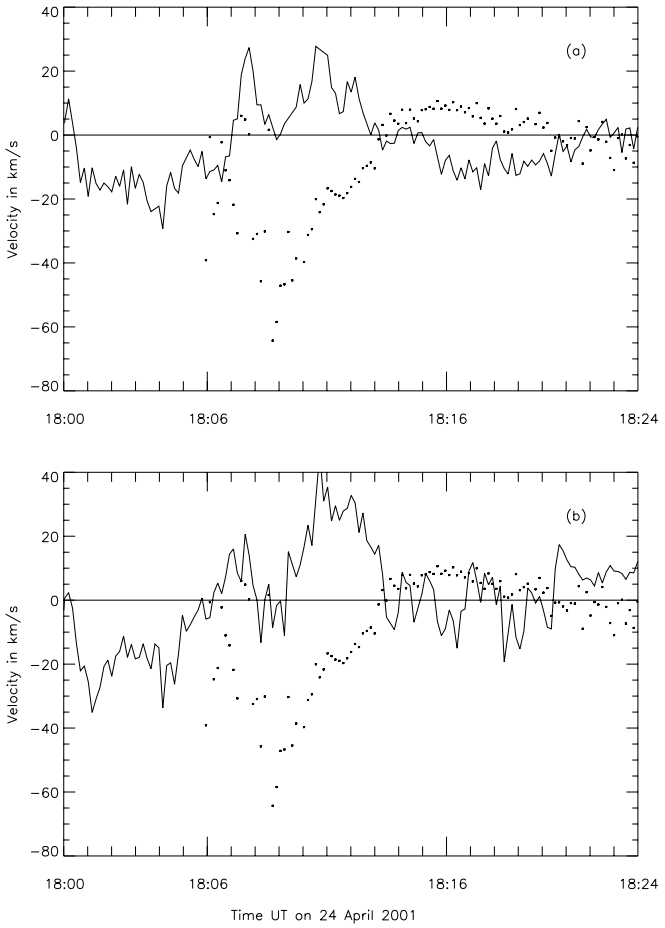

FIG. 8.—Comparison of Doppler velocity measured for Fe XIX (*dots*) and (*a*) He II (*solid line*) and (*b*) O V (*solid line*) for the flare impulsive phase. The close association between downflow (positive) velocities in the cool lines and upflow (negative) velocities in Fe XIX indicates conservation of momentum, as expected in chromospheric evaporation theory.

4. DISCUSSION

The onset of the flare precursors seen in the cooler EUV lines preceded the slow steady rise of the Fe XIX emission by at least 10 minutes (and the Fe XIX intensity spike, barely significant, by about 2 minutes). This indicates that the precursors constituted a chromospheric response to flare energy released; if the precursors were a direct manifestation of flare energy released in the corona, they would have been seen in Fe XIX first. In addition, the impulsive intensity rise of the cooler lines preceded that of Fe XIX by 1.5 minutes, further indicating a chromospheric response to flare energy release rather than a direct measure of the coronal release itself. This suggests, further, that particle beams dominated thermal conduction as the mechanism by which flare energy in this event was transported from its coronal release site to the chromosphere. If thermal conduction dominated, the impulsive intensity rise would be seen in the hotter lines first as the conduction front moved from greater to lower heights (larger to smaller temperatures) in the solar atmosphere. This is true because Fe XIX–emitting plasma is already observed before the impulsive intensity rise, so the passage of a thermal conduction front from the corona to the chromosphere would add to the Fe XIX–emitting plasma (and hence the Fe XIX intensity) before it reached the O III and O V source. (Carrying this a step further, one might expect to see a decrease in the intensities of successively cooler lines as the conduction front passes through and ionizes their emitting volumes along its path; we do not see this during the impulsive intensity rise.) Particle beams, on the other hand, experience much greater stopping in the cooler, denser, plasma that occurs lower down than they do in the corona (e.g., Fig. 1 in Brosius et al. 1995) and so deposit much more of their energy in the chromosphere or lower transition region than they do in the corona. Particle beams essentially traverse the corona unscathed and deposit their energy in the cooler plasma at greater depth.

The sudden rapid rise in the upflow velocity of very hot plasma ($\sim$10 MK as seen, e.g., in Fe XIX, S XV, and Ca XIX) during the flare impulsive phase is generally recognized as the signature of chromospheric evaporation. It is understood, however, that the momentum in this upflowing material must be balanced by a corresponding downflow in underlying (presumably cooler) plasma (e.g., Zarro et al. 1988a; Canfield et al. 1990; Plunkett & Simnett 1994). We measure such

downflows ($\sim$40 km s^{-1}) in the cooler EUV lines observed in this study. That these downflows occur simultaneously with the measured upflows in the hotter lines during the impulsive phase strongly suggests that the downflows are in fact associated with the requisite momentum balance. (Although Cheng [1978, 1980] measured downflows of $\sim$12–70 km s^{-1} in transition-region lines observed during flares with *Skylab*, no corresponding measurements were available for lines formed at $\sim$10 MK.) There is a small time lag ($\sim$1 minute) between the onset of upflows in the hot lines and downflows in the cooler lines, likely due to the fact that it takes awhile to build up sufficient momentum in the downflowing plasma for us to be able to measure the Doppler shift. (The upflowing plasma itself starts out slow and its source not very intense.) The redshifts in the cooler lines stop when the blueshifts in the hotter lines do. The small but significant redshift seen in Fe XIX after the flare impulsive phase (during the peak in the Fe XIX emission) may be due to flare plasma falling back down as ''hot rain'' after the cessation of energy release. Subsequent redshifts seen in the cooler EUV lines provide evidence for ''warm rain'' (see also Brosius 2003) as the flare plasma cools, condenses, and falls back down.

It has become customary to associate chromospheric evaporation (and its incumbent upflows) with hot (10 MK) plasma during the flare impulsive phase. Here, however, we measure significant ($\sim$40 km s^{-1}) upflows in cooler EUV lines, formed at temperatures as low as 10^5 K, during flare precursor events. Further, the rapid EUV intensity rise observed during the precursors is very similar to (but less intense than) that observed during the flare's impulsive phase. Thus the precursors appear to be due to chromospheric evaporation on a smaller scale, suggesting that the same mechanism that gives rise to the behavior observed in the 10 MK plasma during the flare impulsive phase also functions during the flare precursors.

Indeed, in their hydrodynamic simulations of the response of a flare loop atmosphere to thick-target electron heating, Fisher et al.(1985a, 1985b, 1985c) found an energy flux threshold above which chromospheric evaporation is ''explosive'' and below which it is comparatively gentle. (''Thick-target'' simulations refer to those in which the atmosphere is heated by Coulomb collisions with an input flux of nonthermal electrons.) Explosive evaporation occurs when chromospheric plasma is heated much faster than it can radiatively cool. The temperature in the evaporated region jumps to coronal values in a very short time, and the resulting pressure exceeds that in both the overlying corona and the underlying chromosphere. The high gradients on either side of this pressure maximum drive material simultaneously upward into the corona and downward into the chromosphere (Fisher et al. 1985c). Explosive evaporation is effective at driving coronal mass motions to velocities of hundreds of km s^{-1}, while gentle evaporation yields lower upflow velocities. Of greatest interest for our CDS observations, however, are the Fisher et al. (1985b) velocity calculations for plasma at transition-region temperatures ($\sim 10^5$ K). They find that the direction of the transition-region velocity changes at the energy flux threshold, being upward $\sim$20 km s^{-1} for low-energy fluxes (gentle evaporation) and downward near 40 km s^{-1} for high fluxes (explosive evaporation). Recall that the EUV lines of O III, O IV, O V, and He II (formed at transition-region temperatures) observed by CDS exhibit upflows of $\sim$40 km s^{-1} during the two flare precursor events, while the same lines show downflows of $\sim$40 km s^{-1} during the flare impulsive phase. This is consistent with gentle chromospheric evaporation occurring during the two precursors and explosive evaporation during the impulsive phase.

Based on *Yohkoh* SXT images and *GOES* data, Farnik et al. (1996) found that precursors occurred in at least 15% of their flare sample, and in at most 41%. Further, Farnik et al. (1996) found that when flare precursors did occur, they generally did so at locations different from the main phase. On the basis of our CDS and coordinated observations, however, we find that two precursors occur in the same location as the onset of the main phase of our flare on 2001 April 24. If, as we discuss above, the precursors are due to gentle chromospheric evaporation produced by relatively weak beams of nonthermal particles, the solar atmosphere at the flare site will be modified by those beams. (Although one might expect that such beams would produce hard X-ray emission, such emission was not observed by *Yohkoh*'s HXT in our case. It is possible, but beyond the scope of the present study to demonstrate, that this expected hard X-ray emission may be below the sensitivity of HXT.) In any case, the gently upflowing material will increase the density and the column depth of the material through which any subsequent beams must traverse before they can impinge the chromosphere. Thus the solar flare atmosphere will respond differently during the impulsive phase than it would if it had not been subjected to the precursors. This has been investigated by Emslie et al. (1992), whose hydrodynamic numerical simulations of preheated (as by precursors) solar flare atmospheres reveal that the upward velocity of the hydrodynamic gas is reduced by the combination of enhanced coronal column depth (which reduces the amount of energy that can reach the chromosphere) and the increased inertia of the overlying material. Specifically, they find that when the preflare atmosphere is heated such that the coronal density exceeds 6×10^{10} cm^{-3} at flare onset, the upflow velocity of the evaporated material remains smaller than 100 km s^{-1}. This is consistent with the maximum upflow velocities of the 10 MK evaporated material that we measure with both CDS (64 km s^{-1} for Fe XIX) and BCS (65 km s^{-1} for Ca XIX, and 78 km s^{-1} for S XV).

Based upon the emission line list in CHIANTI version 4.2 (Dere et al. 1997; Young et al. 2003), it appears that the Mg X lines at 609.8 and 624.9 Å are sufficiently blended with O IV in their red wings that redshifts unrelated to mass motions may be measured. The Mg X line at 609.79 Å is well known to be blended with an O IV line at 609.83 Å, while the Mg X line at 624.9 Å appears to be blended with O IV lines at 625.1 and 625.8 Å. While the latter of these two appears to be separable (e.g., Brosius 2003), the former is much more problematic. Thus, although Brosius (2003) was able to derive reliable upflow velocities for multiple highly blueshifted components of Mg X at 624.9 Å observed during a *GOES* class M6 flare with a filament liftoff and a CME, we have not been able to do so for this event in which the mass flows are much slower. Here we find that both of the Mg X lines fail to return to their preflare wavelengths late during the flare (they both remain significantly redshifted). While it is possible that these persistent lingering redshifts could also indicate warm rain, the other cool EUV lines all return to their preflare values at the same time. This, combined with the fact that observed intensity ratios of the Mg X lines do not match their theoretical (expected) values, especially during the precursors and the flare, indicates that the lines are contaminated and strengthens our case against using velocity measurements derived from them. This is disappointing, since the Mg X lines are relatively strong and easily observed. For future observations we will use the Si XII ($\log T_m = 6.3$) line at 520.7 Å in order to derive flare Doppler velocities.

5. SUMMARY

We have presented high time resolution EUV and soft X-ray spectroscopic measurements, along with EUV imagery and hard X-ray measurements, of a flaring solar active region loop. The CDS slit was centered directly above the site of flare commencement, which corresponds to the positive magnetic polarity footpoint of the loop. Our results are summarized as follows:

1. The average wavelengths of the O III, O IV, O V, Ne VI, and He II lines measured during the preflare quiescent phase are equal (within the measurement uncertainties) to those measured during the gradual decline phase. This means that the preflare (and gradual decline) wavelengths can be used as reference standards against which to measure Doppler velocities during the flare.
2. The EUV lines of O III, O IV, O V, and He II exhibit upflows of $\sim$40 km s^{-1} during the two flare precursor events.
3. The Fe XIX EUV intensity begins a slow steady rise late during the first precursor event, and it rises and stays above its preflare noise level during the second (later) precursor.
4. The maximum upflow velocities measured in Fe XIX with CDS (64 km s^{-1}) and in Ca XIX (65 km s^{-1}) and S XV (78 km s^{-1}) with BCS occur during the flare impulsive phase and are simultaneous within the instrumental time resolutions (9.83 s for CDS and 9.00 s for BCS).
5. The Fe XIX emission begins its impulsive intensity rise nearly 1.5 minutes after the cooler EUV lines begin theirs.
6. Hard X-ray emission begins to rise nearly 60 s after the cool EUV lines begin their impulsive intensity rise.
7. The EUV lines of O III, O IV, O V, and He II exhibit downflows of $\sim$40 km s^{-1} during the flare impulsive phase.

We interpret our observations in terms of chromospheric evaporation, whose signature is generally recognized as the sudden rapid rise in the upflow velocity of the $\sim$10 MK plasma (as seen in the Fe XIX, S XV, and Ca XIX emission) during the flare impulsive phase. Our observation of simultaneous downflows in the cooler EUV lines provides strong evidence for momentum balance between the hot upflowing material and the cool downflowing material during the flare impulsive phase. Upflows observed in the cooler EUV lines during the two precursor events suggest that chromospheric evaporation occurs then too, only on a smaller scale than during the impulsive phase. The directions and magnitudes of our measured velocities are consistent with those derived in the hydrodynamic simulations of Fisher et al. (1985a, 1985b, 1985c) and Emslie et al. (1992). We find, unfortunately, that the Mg X lines are too blended with O IV emission to provide reliable Doppler velocity measurements; perhaps the strong line of Si XII at 520.7 Å would provide a valuable diagnostic of flare plasma motions at $T \sim 2$ MK in future observations.

We thank Satoshi Morita for valuable assistance with the HXT data analysis. J. W. B. gratefully acknowledges NASA support through the Sun-Earth Connection Guest Investigator Program (NAG5-11757). K. J. H. P. gratefully acknowledges the National Research Council for his Senior Research Associateship. CHIANTI is a collaborative project involving the NRL (USA), RAL (UK), and the Universities of Florence (Italy) and Cambridge (UK). The anonymous referee provided insightful, valuable comments.

REFERENCES

Acton, L. W., et al. 1980, Sol. Phys., 65, 53
Antonucci, E., Alexander, D., Culhane, J. L., de Jager, C., MacNeice, P., Somov, B. V., & Zarro, D. M. 1999, in The Many Faces of the Sun, ed. K. T. Strong, et al. (New York: Springer), 331
Antonucci, E., & Dennis, B. R. 1983, Sol. Phys., 86, 67
Antonucci, E., et al. 1982, Sol. Phys., 78, 107
Bornmann, P. L. 1999, in The Many Faces of the Sun, ed. K. T. Strong et al. (New York: Springer), 301
Brosius, J. W. 2001, ApJ, 555, 435
———. 2003, ApJ, 586, 1417
Brosius, J. W., Robinson, R. D., & Maran, S. P. 1995, ApJ, 441, 385
Canfield, R. C., Zarro, D. M., Metcalf, T. R., & Lemen, J. R. 1990, ApJ, 348, 333
Cheng, C.-C. 1978, Sol. Phys., 56, 205
———. 1980, Sol. Phys., 65, 283
———. 1999, in The Many Faces of the Sun, ed. K. T. Strong, et al. (New York: Springer), 393
Culhane, J. L., et al. 1991, Sol. Phys., 136, 89
Czaykowska, A., De Pontieu, B., Alexander, D., & Rank, G. 1999, ApJ, 521, L75
Delaboudinière, J.-P., et al. 1995, Sol. Phys., 162, 291
Dere, K. P., Landi, E., Mason, H. E., Monsignori-Fossi, B. C., & Young, P. R. 1997, A&AS, 125, 149
Doschek, G. A. 1990, ApJS, 73, 117
Emslie, A. G., Li, P., & Mariska, J. T. 1992, ApJ, 399, 714
Farnik, F., Hudson, H., & Watanabe, T. 1996, Sol. Phys., 165, 169
Fisher, G. H., Canfield, R. C., & McClymont, A. N. 1985a, ApJ, 289, 414
———. 1985b, ApJ, 289, 425
Fisher, G. H., Canfield, R. C., & McClymont, A. N. 1985c, ApJ, 289, 434
Fludra, A., Lemen, J. R., Jakimiec, J., Bentley, R. D., & Sylwester, J. 1989, ApJ, 344, 991
Handy, B. N., et al. 1999, Sol. Phys., 187, 229
Harrison, R. A., et al. 1995, Sol. Phys., 162, 233
Kosugi, T., et al. 1991, Sol. Phys., 136, 17
Mariska, J. T. 1994, ApJ, 434, 756
Mariska, J. T., Doschek, G. A., & Bentley, R. D. 1993, ApJ, 419, 418
Mazzotta, P., Mazzitelli, G., Colafrancesco, S., & Vittorio, N. 1998, A&AS, 133, 403
Neupert, W. M. 1968, ApJ, 153, L59
Pike, C. D., & Mason, H. E. 2002, Sol. Phys., 206, 359
Plunkett, S. P., & Simnett, G. M. 1994, Sol. Phys., 155, 351
Sato, J., Sawa, M., Yoshimura, K., Masuda, S., & Kosugi, T. 2003, The *Yokoh* HXT/SXT Flare Catalogue (Bozeman: Montana State Univ; ISAS)
Scherrer, P. H., et al. 1995, Sol. Phys., 162, 129
Silva, A. V. R., Wang, H., Gary, D. E., Nitta, N., & Zirin, H. 1997, ApJ, 481, 978
Thompson, W. T., 1999, CDS Software Note 53, http://solg2.bnsc.rl.ac.uk/software/notes.shtml
Tsuneta, S., et al. 1991, Sol. Phys., 136, 37
Woodgate, B. E., et al. 1980, Sol. Phys., 65, 73
Young, P. R., Del Zanna, G., Landi, E., Dere, K. P., Mason, H. E., & Landini, M. 2003, ApJS, 144, 135
Zarro, D. M., Canfield, R. C., Strong, K. T., & Metcalf, T. R. 1988a, ApJ, 324, 582
Zarro, D. M., Slater, G. L., & Freeland, S. L. 1988b, ApJ, 333, L99